

## Quantifying order in breath figure patterns through Voronoi entropy

David Paulovics <sup>1,\*</sup>, Edward Bormashenko <sup>2</sup>, Christophe Raufaste <sup>1,3</sup> and Franck Celestini<sup>1</sup>

<sup>1</sup>*Université Côte d'Azur, CNRS, Institut de Physique de Nice, 06200 Nice, France*

<sup>2</sup>*Engineering Faculty, Chemical Engineering, Biotechnology and Materials Department, Ariel University, Ariel*

<sup>3</sup>*Institut Universitaire de France (IUF), 75005 Paris, France*

 (Received 15 November 2023; revised 24 June 2024; accepted 17 July 2024; published 2 August 2024)

In this study, we simulate breath figures that are evolving two-dimensional assemblies of droplets on a substrate. We focus on the Voronoi/Shannon entropy of these figures, which quantifies the order related to the coordination number of droplets. We show that the Voronoi entropy of the complete breath figure pattern converges to a value that is the one of a randomly distributed point system. Conversely, the subset containing exclusively large droplets of the breath figure exhibits significantly lower entropy than that obtained for all droplets. Using molecular dynamics simulations, we show that coalescence events in breath figures induce the same Voronoi entropy as that caused by repulsive interactions in a bidimensional atomic system.

DOI: [10.1103/PhysRevE.110.024302](https://doi.org/10.1103/PhysRevE.110.024302)

### I. INTRODUCTION

Water condensation is an extremely important process in Earth's water cycle [1] and appears when air is cooled to its saturation limit. From the formation of clouds which affects the climate system to the use of air wells and fog fences to collect water [2] through the formation of frost on solid surfaces [3–5], it has a direct impact on human activities. The condensation process on a cold substrate takes place according to two main physicochemical scenarios. Dropwise condensation is characterized by individual droplets appearing on the solid surface, while filmwise condensation consists of a thin and continuous water film coating the substrate [6,7]. The first scenario is the origin of microscopic droplet arrangements, called breath figures, that explain why a mirror gets foggy in the bathroom or why cold glasses become opaque in a humid environment. Studies on breath figures were conducted as far back as a century ago by Rayleigh, Aitken, and Baker [8–12]. In particular, Aitken discovered that filmwise water condensation took place on the glass surface treated with a blowpipe flame, whereas dropwise condensation occurred on the nontreated surface of the same glass [8,9]. Nowadays, dropwise condensation is at the origin of applications such as polymer film micropatterning and functionalization [13–17].

The pattern made of the droplet arrangement inside a breath figure depends on the substrate geometry and properties [18–20]. It is the result of a complex interplay of various physicochemical phenomena, including water droplet nucleation, growth, and coalescence. Breath figures go through three stages throughout their temporal evolution [21]. This has been observed for growth on a solid surface [22], on a liquid interface [23], and also in simulations [24].

These stages are as follows: (i) A first stage with low surface coverage and rare droplet interactions. (ii) An intermediate stage, characterized by high values of surface coverage,

with frequent interaction between small droplets. (iii) A final and dense scaling regime for the droplet size distribution whose average radius increases with time [25]. This distribution is bimodal with one part associated with small droplets formed by nucleation and a small degree of coalescence with other droplets, and one part associated with large droplets resulting from the coalescence of many droplets. Condensation droplets on solid substrates interact solely through coalescence, inhibiting the formation of highly ordered patterns. Nonetheless, measurements of the pair distribution function in these systems reveal that the pattern develops spatial correlations and exhibits short-range ordering, reaching a maximum in the scaling regime [26]. In contrast, condensation droplets on the surface of a liquid can interact with mechanisms other than coalescence, leading to varying degrees of translation and orientation orders during the breath figure time evolution [23].

Our study aims to quantify the order related to the coordination number of droplets on solid surfaces across the successive stages of time evolution, ranging from the initial patterns composed of scarce and small droplets to the final scaling regime with a bimodal radius distribution. To quantify this order, we employ the Voronoi/Shannon entropy [21,23,27–33].

At first, we measured the time evolution of the Voronoi entropy within breath figures from the initial nucleation events to the scaling regime. Our approach is numerical following the scheme introduced by Family and Meakin [25]. We define two distinct sets of droplets, the first being all droplets composing the breath figure, the second one consisting exclusively of large droplets. For all droplets, the time evolution of Voronoi entropy occurs in two distinct stages. First, during the initial nucleation events, coalescence between small and monodisperse droplets induces a decrease in entropy. Second, at large times, the entropy increases back to a value characteristic of a random point system. This increase in entropy is attributed to the inherent bidisperse nature of a breath figure. The situation is rather different looking at the entropy of solely large droplets. In the case of this set, the entropy decreases

\*Contact author: david.paulovics@univ-cotedazur.fr

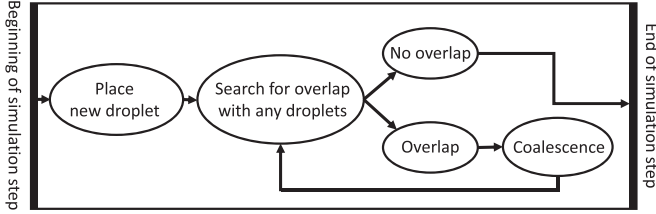


FIG. 1. Diagram of one simulation step of the droplet deposition algorithm.

and reaches a limiting value significantly lower than the one measured for all droplets.

Finally, we performed molecular dynamics simulations of a bidimensional Lennard-Jones fluid at different temperatures and densities. We first show that the initial decrease in entropy for all droplets of a breath figure is the same as the decrease of Entropy in a Lennard-Jones fluid at low densities. It is worth noticing that initial values of Voronoi entropy are the same for the two systems: precisely that obtained for a random point system. Second, we show that the Voronoi entropy of large droplets within breath figures is very close to that of a Lennard-Jones fluid simulated at equivalent density and in the limit of high temperatures where the repulsive atomic interaction is predominant. This highlights how coalescence events in breath figures induce similar values of entropy to that of repulsive interactions in a two-dimensional atomic system.

## II. MATERIALS AND METHODS

### A. Simulations of breath figures

We simulate breath figures (BF) following the numerical scheme depicted by Family and Meakin [25]. Starting with an initially empty  $L \times L$  sized two-dimensional surface, at each simulation step, we place a new droplet of radius  $R_0$  at a random position. Each new droplet has a radius  $R_0$  and a contact angle of  $90^\circ$ , such that it can be represented with the coordinates of the center and the radius of a hemisphere on the surface. We chose  $R_0$  as the unit length and defined a dimensionless time  $t = \frac{\pi R_0^2}{L^2} n$  with  $n$  the number of simulation steps (i.e., the number of deposited unit size droplets). In breath figure simulations we fixed  $L = 2 \cdot 10^3 R_0$ . When a new droplet is placed at a random position two cases can occur:

(i) The droplet does not overlap with any other ones and is kept at this random position.

(ii) It overlaps with another droplet giving rise to a coalescence event. The two droplets are then replaced by a new one, respecting mass, center of mass, and contact angle conservation.

This new droplet can also overlap with others, thus multiple coalescences can occur in one simulation step. Search for overlap is conducted after every coalescence until there are no more overlaps. A diagram of the algorithm is shown in Fig. 1. This simulation therefore reproduces the two mechanisms of three-dimensional droplet growth on a two-dimensional surface: growth due to water molecules coming from the atmosphere and growth due to their coalescence. Some typical images of such breath figures are shown in Fig. 2. In this approach, droplets grow continuously by coalescence, which

freees some space that new droplets can therefore occupy in subsequent time steps. Due to this process, the shape of the radius distribution evolves with time. At earlier times, the probability density function (PDF) of droplet radii is a monotonously decreasing function with a maximum at  $R = 1$ . Such a distribution is illustrated in the inset of Fig. 2(a). At approximately  $t = 1.7$ , the distribution develops a local minimum and becomes bimodal. From this time we can therefore clearly define a time-dependent critical radius  $R_c(t)$  that corresponds to the local minimum of the distribution. Three typical distributions are shown in the insets of Figs. 2(b)–2(d). The value of  $R_c(t)$  is measured and is shown to increase monotonously with time, as shown in Fig. 3(a). The increase is sublinear initially and becomes linear over time after  $t \simeq 3.5$ . This is consistent with the fact that the radius distribution becomes self-similar over time, with an average radius that linearly increases with time, and a bimodal distribution consisting of small and polydisperse droplets for  $R < R_c(t)$  and large and monodisperse droplets for  $R > R_c(t)$  [25].

Based on the previous discussion, we can now consider two distinct sets of droplets. The first one encompasses all droplets of the breath figures, while the second consists exclusively of large droplets with radii larger than  $R_c(t)$ . In the following, the two sets will be referred to respectively as “all droplets” and “large droplets.”

For each set, we define the surface coverage as  $\phi = \frac{\sum_{i=1}^N \pi R_i^2}{L^2}$  where  $N$  is the number of droplets in the set [18,20,22,34]. We also define the density  $\rho = \frac{\sum_{i=1}^N (2R_i)^2}{L^2}$ , which is proportional with a factor of  $4/\pi$  to the surface coverage, to facilitate comparison with simulations of Lennard-Jones fluids. Indeed as will be detailed in Sec. II C, density is defined as  $\rho = \frac{N\sigma^2}{L^2}$ , where  $\sigma$  is the characteristic length of the Lennard-Jones potential that can be assimilated to the diameter of a particle. Surface coverage is plotted in Fig. 3(b). It is a continuously increasing function of time if we consider all droplets. For the set of large droplets defined from  $t = 1.7$ , the surface coverage saturates from  $t \simeq 5$ , in agreement with the onset of the linear trend in  $R_c(t)$  and of the scaling regime for the size distribution. The surface coverage saturates at a value of  $0.572 \pm 0.003$  in agreement with former measurements [34].

### B. Two benchmarks: Random points and nonoverlapping disk deposition

In addition to the simulation of breath figures (BF), we simulated two other systems based on the same approach but with different deposition conditions.

The first case is the simulation of random points (RP). The algorithm is unchanged, but the radius of the particles is assumed to be zero so that coalescence never occurs. This situation corresponds to a random two-dimensional pattern or a random space-filling structure or Poisson points process [35], often cited as a reference in quantifying order or disorder in two-dimensional patterns [21,36,37].

The second case involves simulating nonoverlapping disks, also called a simple sequential inhibition process (SSI) as previously studied by Smalley [38], Diggle *et al.* [39], and Lotwick [40]. In this scenario, we deposit unit-sized droplets

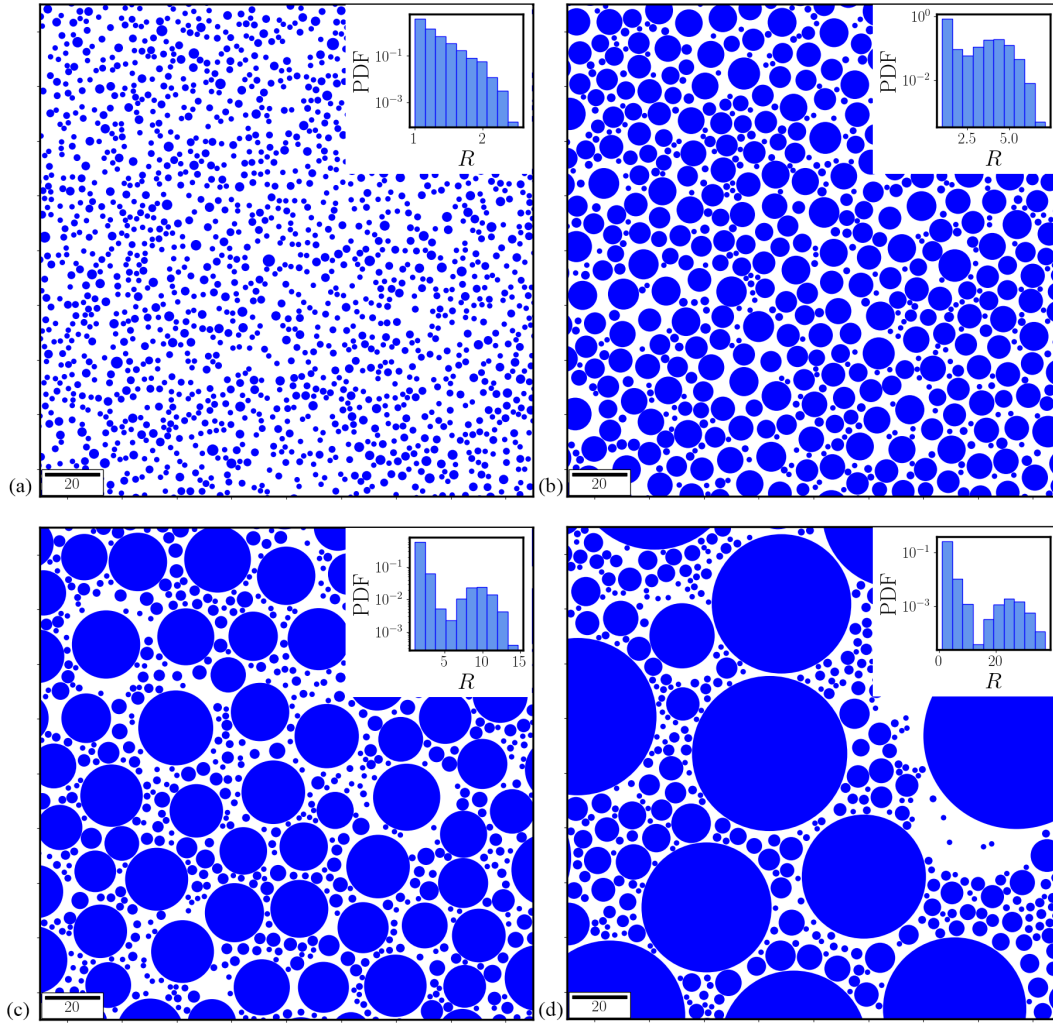


FIG. 2. Crops of typical images of simulated breath figures at  $t = 0.3, 2.5, 6.0,$  and  $16.0$  from left to right and from up to down. The corresponding total number of deposited droplets  $n$  are  $4 \cdot 10^5, 3 \cdot 10^6, 8 \cdot 10^6,$  and  $2 \cdot 10^7$ , while the number of droplets actually present are  $N = 2 \cdot 10^5, 9 \cdot 10^4, 7 \cdot 10^4,$  and  $5 \cdot 10^4$ , respectively. Insets show the corresponding probability distribution functions (PDF) of droplet radii, calculated from the full simulation of size  $2000R_0 \times 2000R_0$ .

randomly, adhering to an exclusion principle that prevents placing a droplet if it intersects with another droplet already present on the substrate. The condition of coalescence of breath figures is replaced in this case by a condition of nondeposition in the SSI simulation. This interaction can be viewed as a coalescence that does not affect the position and size of the already present droplet.

### C. Molecular dynamics simulations

We perform two-dimensional molecular dynamics simulations of particles in a square box of size  $L \times L$ . We note  $m$  the mass of one particle. Two particles separated by a distance  $r$  interact through the Lennard-Jones potential:

$$V(r) = \begin{cases} 4\epsilon \left[ \left( \frac{\sigma}{r} \right)^{12} - \left( \frac{\sigma}{r} \right)^6 \right] & \text{if } r \leq 2.5\sigma \\ 0 & \text{if } r > 2.5\sigma \end{cases} \quad (1)$$

Lengths, energies, and masses are expressed in units of  $\sigma, \epsilon,$  and  $m$  respectively, and times in units of  $m^{1/2}\sigma\epsilon^{-1/2}$ . Without

loss of generality, we take these three constants equal to one. The equations of motion are integrated through a standard Verlet algorithm [41] in the canonical ensemble for which the temperature  $T$  is fixed using the classical velocity rescaling procedure [41]. In this procedure, the Boltzmann constant is fixed to unity and temperatures are expressed in terms of  $\epsilon/k_b$ . We define particle density as  $\rho = \frac{N\sigma^2}{L^2}$ , where  $N$  is the number of particles.

We simulate assemblies of a constant number  $N = 2^{12}$  of particles and the length  $L$  of the simulation box is tuned to set the density to desired values, contrarily to breath figure simulations where  $L$  is always kept constant and the number of particles varies. Periodic boundary conditions are applied in both  $x$  and  $y$  directions. The time step is set to  $dt = 0.002$  or  $0.0002$  depending on density and temperature to ensure energy conservation of our numerical scheme. At higher temperatures, particle velocities and the rate of their interactions is increased, thus, in order to conserve the total energy of the system, we need a smaller timestep. In our range of

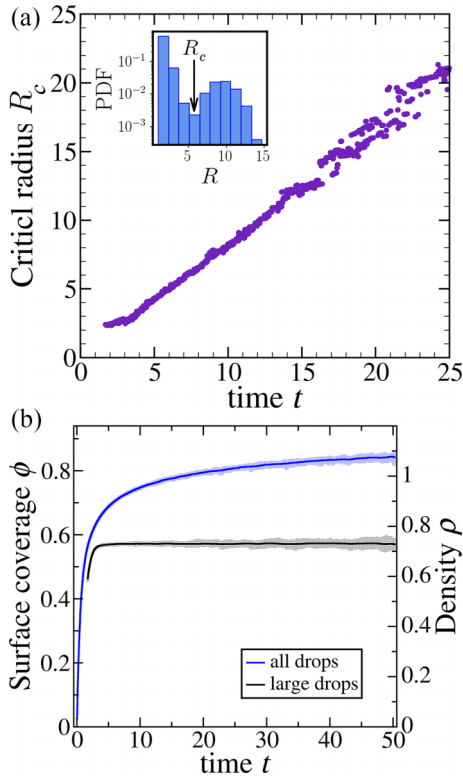


FIG. 3. (a) Time evolution of the critical radius of breath figures. Inset shows an example of probability distribution function (PDF) for  $t = 6$ , figuring  $R_c$ . (b) Plot of  $\rho$  and  $\phi$  as a function of time for both the all droplets and large droplets systems. Plain lines are the results of a running average of the measurements.

parameters, the system is equilibrated during approximately  $10^5$  time steps, and uncorrelated spatial configurations are then recorded every  $10^3$  time steps during a second simulation of  $10^5$  time steps. Simulations are performed for densities varying between 0.05 and 0.8, and temperatures ranging from 1 to 120. We vary  $T$  systematically within this range with a step size of  $\Delta T = 1$ . We limit our study to densities less than 0.8 and temperatures greater than 1.0 in order to restrict the analysis to the liquid phase. Indeed, the liquid-hexatic phase transition is reported to be approximately at  $\rho \simeq 0.88$  for  $T \simeq 1.0$  [42].

#### D. Measurement of Voronoi entropy

Measurement of Voronoi entropy has already been employed to characterize ordering related to coordination numbers of other 2D systems [21,23,27–33]. For a given system on the 2D plane, we build a Voronoi diagram/tessellation based on the set of sites (coordinates of disk centers for droplets in breath figures, particle positions in molecular dynamics simulations) [35,43–45]. This diagram is calculated with a Python script using the `scipy.spatial` repository, integrating the `Qhull` library [46]. It leads to a partitioning of the plane into polygonal regions consisting of all points closer to a site than to any other. This diagram defines the nearest neighbors and the number of sides of a polygon gives the coordination number of a site in the tessellation (see Fig. 4 and Fig. 8

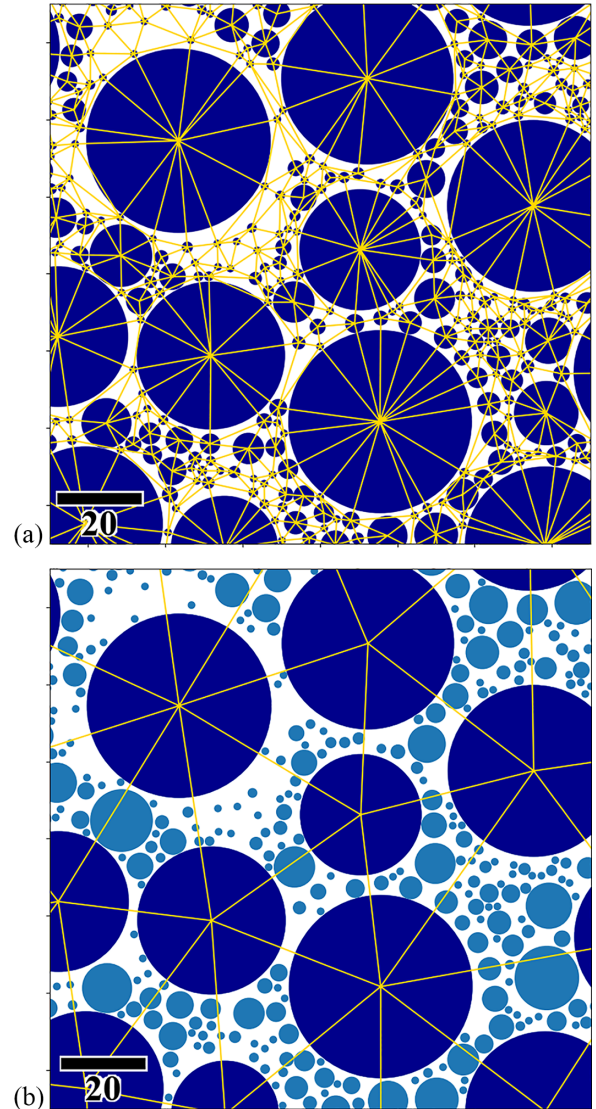


FIG. 4. Example of a Delaunay triangulation that is the dual of a Voronoi tessellation, considering (a) all droplets or (b) large droplets only ( $R > R_c$ ), for  $t = 14$  in breath figure simulations as explained in Sec. II A. The considered droplets are shown in dark blue color, while nonconsidered droplets are in light blue.

for examples of BF with sets made of all droplets and large droplets, respectively, and for LJFs). The Voronoi entropy quantifies the dispersion of polygon side numbers based on Shannon entropy:

$$S = \sum_k -P_k \ln(P_k), \quad (2)$$

with  $P_k$  the probability that a polygon has  $k$  sides or neighbors. If the tessellation is constructed from polygons of the same type, e.g., hexagons, the Voronoi entropy is minimal and equal to zero. The Voronoi entropy increases with the diversity of polygon types present in a given Voronoi diagram. It can be recognized from Eq. (2) that the Voronoi/Shannon entropy quantifies the average unlikelihood or unexpectedness to find polygons with the given number of sides in the addressed Voronoi tessellation. For instance, the Voronoi entropy equals

1.69 for an assembly of random points (see Sec. III A). We calculate  $S$  for BF on 20 independent simulations for both sets of all droplets and large droplets. For molecular dynamics simulations with a Lennard-Jones potential, we calculate  $S$  on 100 uncorrelated particle spatial configurations for each density and temperature value.

### III. RESULTS

#### A. Voronoi entropy of a breath figure

In this section, we calculate the Voronoi entropy  $S$  for the two subsets of a breath figure as defined above: the first subset being all droplets and the second the large droplets. For all droplets,  $S$  starts from a value that is consistent with the one calculated in our random point (RP) simulations ( $S = 1.6904 \pm 0.0005$ ). This value aligns perfectly with results obtained from early simulations of Poisson distributed random points [47]. Nevertheless, it slightly deviates from the value of 1.71 often reported in the literature to characterize such arrangements [21]. We attribute this difference to a possible confusion between random points and hierarchical arrangements also known as compound negative binomial (CNB) distributions [48].

As time increases we observe a decrease of entropy that we interpret as a direct consequence of coalescence events. Then from approximately  $t \simeq 0.7$ , entropy increases and for large times reaches a limit value that is also close to that of an RP system. We attribute this increase in entropy to polydispersity in droplet size. In contrast, the entropy of the second subset consisting solely of large droplets is a decreasing function of time and reaches a steady state value of approximately 1.26, which is sensibly lower than the one observed for all droplets.

A more detailed examination of the entropy of all droplets reveals a more complex behavior. The initial decrease, starting from the RP value, resembles that of the SSI system, as depicted in Fig. 5(b) [a magnification of Fig. 5(a) for low times]. The deviation of the entropy  $S$  for all droplets from that of SSI can be attributed to the polydispersity in droplet size distribution. This polydispersity is present in breath figure simulations while, by definition, it is not in the SSI model. Furthermore,  $S$  for all droplets increases until it surpasses the initial RP value to reach a maximum of 1.71. It is attained due to a hierarchical arrangement within the breath figure, such as in a compound negative binomial (CNB) distribution [48,49]. Indeed, due to the clustering effect, CNB exhibits higher entropy compared to RP. Bidispersity causes the small droplets of the breath figure to cluster between the large droplets. For large values of  $t$ , the entropy  $S$  for all droplets asymptotically approaches the entropy value for RP. This behavior can be explained by the significant reduction in the number of large droplets at large times, roughly  $t > 20$ . In between large droplets, small droplets are arranged randomly, as for initial times. Thus, the value of entropy turns back to that of a random point system.

#### B. Voronoi entropy in Lennard-Jones fluids and comparison with breath figures

We measured the Voronoi entropy  $S$  of Lennard-Jones fluids (LJF) as described in Secs. IIC and IID. In Fig. 6,  $S$  is represented as a function of density for two different

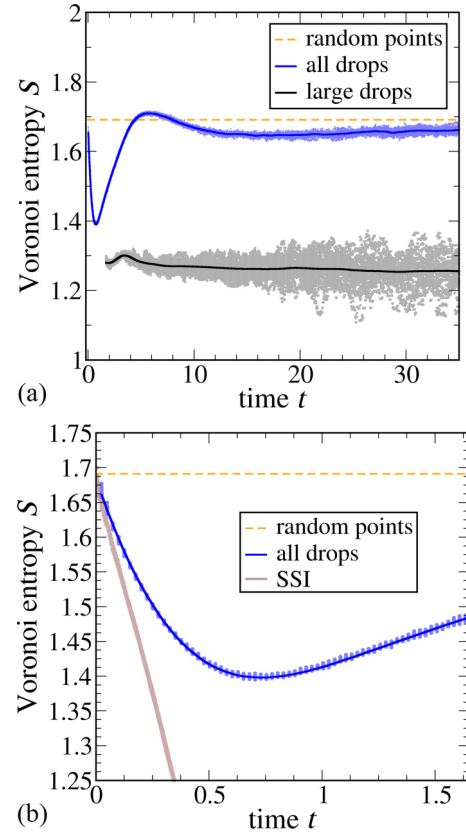


FIG. 5. (a) Time evolution of  $S$  for all droplets (blue) and for large droplets (black). The orange dashed line is placed at the asymptotic value of  $S$  corresponding to an assembly of random points (RP). (b) A zoom on the early instants of the evolution. The brown full curve shows the time evolution of  $S$  for a nonoverlapping random disk system (SSI), explained in Sec. IIB.

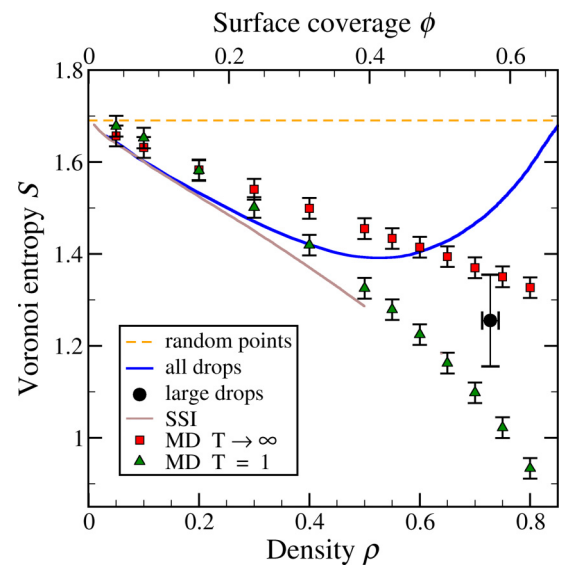


FIG. 6. Comparison of the evolution of  $S$  for BF, MD, RP, and SSI as a function of density and surface coverage. The black dot corresponds to the Voronoi entropy of the large droplets of breath figures at their density of saturation as explained in Sec. IIA.

temperatures. We plotted the results for  $T = 1$  and  $T = 100$  that correspond to results at intermediate and infinite temperatures, respectively. Some snapshots of the simulation for different densities and temperatures are presented in Fig. 7 of the Appendix.

Regardless of temperature, the limit  $\rho \rightarrow 0$  gives a value of  $S$  very close to 1.69, which is the value expected for a random point system. At a given temperature, the Voronoi entropy is a decreasing function of density, and for a given density, the lower the temperature the lower the entropy. For  $T = 1$  the effect of the attractive part of the interaction results in a stronger decrease of  $S$  as  $\rho$  increases. As discussed in Sec. II C, this behavior marks the onset of the liquid-to-hexatic transition.

At low densities ( $\rho < 0.2$ ), the Voronoi entropy displays the same decreasing trend as a function of density for all models considered: BF, SSI, and LJF at high and low temperatures. It seems reasonable to associate the increase of density with an increase in the probability of particles or droplets interacting, thus to a decrease of entropy. We know that in the case of BF and SSI, this interaction is coalescence. The entropy for LJF displays this same decreasing behavior at large temperatures, where the repulsive part of the potential is predominant. As a consequence, we can conclude that coalescence events in BF can be viewed as an effective repulsive interaction, just as it is the case of a high-temperature Lennard-Jones fluid.

Around  $\rho \simeq 0.4$  the Voronoi entropy of all droplets of BF (blue curve in Fig. 6) is increasing with density. This behavior is analogous to that described and explained in Sec. III A. It deviates from SSI and LJF because of the polydispersity in droplet size. This is no longer the case if we consider the entropy of the large droplets of BF. The density and entropy variations are small for this set of droplets, and both quantities quickly reach their steady-state values corresponding to the scaling regime. For this reason, we represented in Fig. 6 the entropy for large droplets by a single point with error bars. Dispersion in measurements of entropy is due to finite system size. One can observe that the value of entropy for large droplets compares well with that of a Lennard-Jones fluid in the limit of high temperatures (typically  $T > 10.0$ ) and at a density equal to that of the asymptotic density of the large droplets of a BF ( $\rho = 0.72$ ). One can conclude that while all droplets of a BF behave similarly to a random system, the set consisting of large droplets exhibits a Voronoi entropy consistent with that of a high-temperature Lennard-Jones fluid where repulsive interactions are predominant.

**IV. CONCLUSION**

In this paper, we have quantified the time evolution of the Voronoi entropy of breath figures by performing numerical simulations, taking into account deposition and coalescence processes. When considering the entire set of droplets, the entropy starts at 1.69, which is the value one would expect for a random point system. However, it then undergoes a complex evolution linked to the interaction between droplets, namely coalescence becoming more important as surface coverage increases, as well as changes in polydispersity as the system’s density increases. Ultimately, it asymptotically

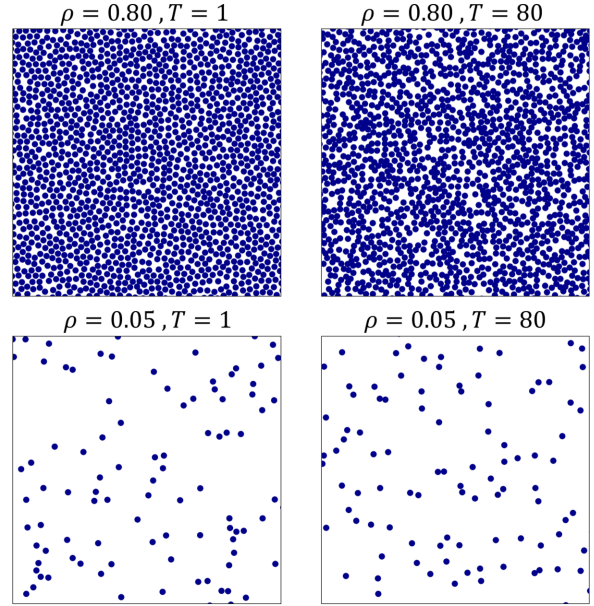


FIG. 7. Snapshots of particles molecular dynamics simulations of varying densities and temperatures. Images of the first row are at  $\rho = 0.8$  and those at the second row are at  $\rho = 0.05$ . The first column is at  $T = 1$ , while the second is at  $T = 80$ . All images show particles in a window of size  $(48 \times 48)\sigma$ . The particles are represented by blue disks whose diameter is  $\sigma$ .

returns to a value of 1.69, that of a random point system as the pattern becomes self-similar. In contrast, the set comprised solely of large droplets resulting from numerous coalescence events demonstrates a lower entropy of a value of 1.26.

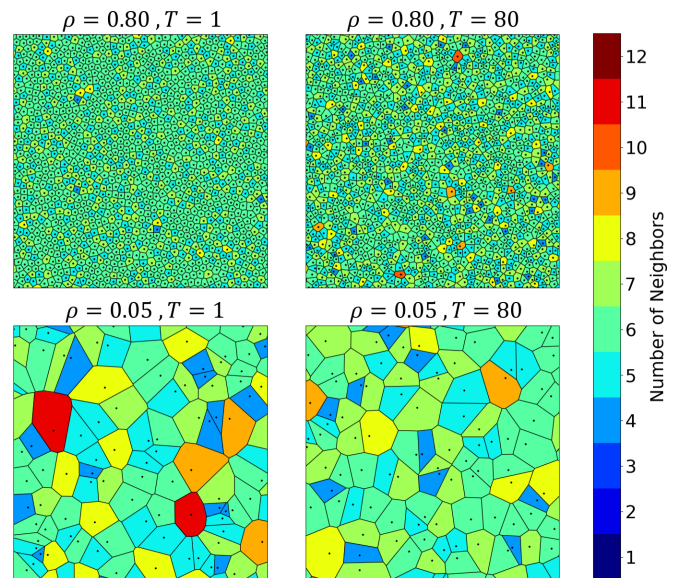


FIG. 8. Voronoi tessellations calculated from particle positions shown in Fig. 7. The colors of the Voronoi polygons represent their coordination number according to the colorbar on the right.

We have also characterized the evolution of the Voronoi entropy of simulated Lennard-Jones fluids as a function of density and temperature. We compared the data obtained for breath figures with that coming from molecular simulations of Lennard-Jones fluids at various temperatures. We demonstrated by this comparison that the order related to the coordination number observed in the set of large droplets of breath figures is similar to that observed in atomic systems in the limit of high temperatures ( $T > 40$ ), where attractive energies and forces are not at play [50].

Consequently, coalescence events can be regarded as effective repulsive interactions in breath figures from the perspective of Voronoi entropy, which quantifies the ordering related to the coordination number.

#### APPENDIX: VORONOI TESSELATIONS OF LJ FLUIDS

Figure 7 shows snapshots of molecular dynamics simulations for two different densities at two different temperatures as explained in Sec. II C. For high density ( $\rho = 0.8$ ) at high temperature ( $T = 80$ ), a larger dispersion in the coordination number of particles is apparent in Fig. 8 compared to the snapshot at the same density at low temperature ( $T = 1$ ). This is consistent with the corresponding values of Voronoi entropies presented in Fig. 6. Conversely, at low density ( $\rho = 0.05$ ) and low temperature ( $T = 1$ ), a high dispersion is observable, due to the presence of a very slight clustering effect between particles. This also aligns with the Voronoi entropy values discussed in the article.

- 
- [1] M. T. Chahine, *Nature (London)* **359**, 373 (1992).
- [2] M. Fessehaye, S. A. Abdul-Wahab, M. J. Savage, T. Kohler, T. Gherezghiher, and H. Hurni, *Renew. Sustain Energy Rev.* **29**, 52 (2014).
- [3] S. Nath, S. F. Ahmadi, and J. B. Boreyko, *Nanoscale Micros. Thermophys. Eng.* **21**, 81 (2017).
- [4] D. Paulovics, C. Raufaste, T. Frisch, C. Claudet, and F. Celestini, *Langmuir* **38**, 2972 (2022).
- [5] S. Curiotto, D. Paulovics, C. Raufaste, F. Celestini, T. Frisch, F. Leroy, F. Cheynis, and P. Müller, *Langmuir* **39**, 579 (2023).
- [6] D. G. Wilkins, L. A. Bromley, and S. M. Read, *AIChE J.* **19**, 119 (1973).
- [7] B. El Fil, G. Kini, and S. Garimella, *Int. J. Heat Mass Transf.* **160**, 120172 (2020).
- [8] J. Aitken, *Proc. Roy. Soc. Edinb.* **20**, 94 (1895).
- [9] J. Aitken, *Nature (London)* **86**, 516 (1911).
- [10] Rayleigh, *Nature (London)* **86**, 416 (1911).
- [11] Rayleigh, *Nature (London)* **90**, 436 (1912).
- [12] T. Baker, *The London, Edinburgh, and Dublin Philos. Mag. J Sci.* **44**, 752 (1922).
- [13] G. Widawski, M. Rawiso, and B. François, *Nature (London)* **369**, 387 (1994).
- [14] B. François, O. Pitois, and J. François, *Adv. Mater.* **7**, 1041 (1995).
- [15] J. Rodríguez-Hernández and E. Bormashenko, *Breath Figures* (Springer International Publishing, Cham, 2020).
- [16] M. Srinivasarao, D. Collings, A. Philips, and S. Patel, *Science* **292**, 79 (2001).
- [17] H. Yabu, M. Tanaka, K. Ijro, and M. Shimomura, *Langmuir* **19**, 6297 (2003).
- [18] D. Beysens, A. Steyer, P. Guenoun, D. Fritter, and C. M. Knobler, *Phase Trans.* **31**, 219 (1991).
- [19] D. Beysens, *Atmos. Res.* **39**, 215 (1995).
- [20] D. Beysens, *C. R. Phys. Nucleation* **7**, 1082 (2006).
- [21] A. V. Limaye, R. D. Narhe, A. M. Dhote, and S. B. Ogale, *Phys. Rev. Lett.* **76**, 3762 (1996).
- [22] D. Beysens and C. M. Knobler, *Phys. Rev. Lett.* **57**, 1433 (1986).
- [23] A. Steyer, P. Guenoun, D. Beysens, and C. M. Knobler, *Phys. Rev. B* **42**, 1086 (1990).
- [24] D. Fritter, C. M. Knobler, D. Roux, and D. Beysens, *J. Stat. Phys.* **52**, 1447 (1988).
- [25] F. Family and P. Meakin, *Phys. Rev. A* **40**, 3836 (1989).
- [26] D. Fritter, C. M. Knobler, and D. A. Beysens, *Phys. Rev. A* **43**, 2858 (1991).
- [27] P. Moriarty, M. D. R. Taylor, and M. Brust, *Phys. Rev. Lett.* **89**, 248303 (2002).
- [28] C. P. Martin, M. O. Blunt, and P. Moriarty, *Nano Lett.* **4**, 2389 (2004).
- [29] A. Stannard, *J. Phys.: Condens. Matter* **23**, 083001 (2011).
- [30] J. Ding, A. Zhang, H. Bai, L. Li, J. Li, and Z. Ma, *Soft Matter* **9**, 506 (2013).
- [31] F. Galeotti, F. Trespidi, G. Timò, and M. Pasini, *ACS Appl. Mater. Interfaces* **6**, 5827 (2014).
- [32] V. Lotito and T. Zambelli, *Langmuir* **34**, 7827 (2018).
- [33] E. Bormashenko, M. Frenkel, A. Vilck, I. Legchenkova, A. A. Fedorets, N. E. Aktaev, L. A. Dombrovsky, and M. Nosonovsky, *Entropy* **20**, 956 (2018).
- [34] P. Meakin, *Rep. Prog. Phys.* **55**, 157 (1992).
- [35] D. Weaire and N. Rivier, *Contemp. Phys.* **25**, 59 (1984).
- [36] E. Bormashenko, I. Legchenkova, and M. Frenkel, *Entropy* **21**, 452 (2019).
- [37] M. Frenkel, I. Legchenkova, N. Shvalb, S. Shoval, and E. Bormashenko, *Symmetry* **15**, 746 (2023).
- [38] I. J. Smalley, *Geolog. Mag.* **103**, 110 (1966).
- [39] P. J. Diggle, J. Besag, and J. T. Gleaves, *Biometrics* **32**, 659 (1976).
- [40] H. Lotwick, *J. Stat. Comput. Simul.* **15**, 295 (1982).
- [41] M. P. Allen and D. J. Tildesley, *Computer Simulation of Liquids* (Oxford University Press, Oxford, UK, 2017).
- [42] A. Hajibabaei and K. S. Kim, *Phys. Rev. E* **99**, 022145 (2019).
- [43] G. Voronoi, *J. für die reine und angewandte Mathematik (Crelles Journal)* **1908**, 198 (1908).
- [44] M. Barthélemy, *Phys. Rep.* **499**, 1 (2011).
- [45] E. Bormashenko, I. Legchenkova, M. Frenkel, N. Shvalb, and S. Shoval, *Entropy* **25**, 92 (2023).

- [46] P. Virtanen, R. Gommers, T. E. Oliphant, M. Haberland, T. Reddy, D. Cournapeau, E. Burovski, P. Peterson, W. Weckesser, J. Bright, S. J. van der Walt, M. Brett, J. Wilson, K. J. Millman, N. Mayorov, A. R. J. Nelson, E. Jones, R. Kern, E. Larson, C. J. Carey *et al.*, [Nat. Methods](#) **17**, 261 (2020).
- [47] I. K. Crain, [Comput. Geosci.](#) **4**, 131 (1978).
- [48] K. Ord and A. Rogers, *Statistical Analysis of Spatial Dispersion* (Cambridge University Press, Cambridge, 1974).
- [49] B. Boots, [Metallography](#) **15**, 53 (1982).
- [50] R. Tadmor and J. Klein, [J. Colloid Interface Sci.](#) **247**, 321 (2002).